

Cryo-EM analysis of *S. aureus* TarL, a polymerase in wall teichoic acid biogenesis central to virulence and antibiotic resistance

Franco K. K. Li^{1,2}, Liam J. Worrall^{1,2}, Robert T. Gale³, Eric D. Brown³, Natalie C. J. Strynadka^{1,2*}

Wall teichoic acid (WTA), a covalent adduct of Gram-positive bacterial cell wall peptidoglycan, contributes directly to virulence and antibiotic resistance in pathogenic species. Polymerization of the *Staphylococcus aureus* WTA ribitol-phosphate chain is catalyzed by TarL, a member of the largely uncharacterized TagF-like family of membrane-associated enzymes. We report the cryo-electron microscopy structure of TarL, showing a tetramer that forms an extensive membrane-binding platform of monotopic helices. TarL is composed of an amino-terminal immunoglobulin-like domain and a carboxyl-terminal glycosyltransferase-B domain for ribitol-phosphate polymerization. The active site of the latter is complexed to donor substrate cytidine diphosphate-ribitol, providing mechanistic insights into the catalyzed phosphotransfer reaction. Furthermore, the active site is surrounded by electropositive residues that serve to retain the lipid-linked acceptor for polymerization. Our data advance general insight into the architecture and membrane association of the still poorly characterized monotopic membrane protein class and present molecular details of ribitol-phosphate polymerization that may aid in the design of new antimicrobials.

Copyright © 2024 The Authors, some rights reserved; exclusive licensee American Association for the Advancement of Science. No claim to original U.S. Government Works. Distributed under a Creative Commons Attribution NonCommercial License 4.0 (CC BY-NC).

INTRODUCTION

Wall teichoic acid (WTA) is an anionic glycopolymer that is covalently attached to the cell wall peptidoglycan of Gram-positive bacteria. WTA confers protection against host defenses by acting as a physical and chemical barrier to host molecules that cleave peptidoglycan (1, 2), disrupt the bacterial cell membrane (3, 4), or promote phagocytosis by leukocytes (5). At the same time, the polymer can interact with various physiological or synthetic molecules to facilitate colonization on a variety of surfaces ranging from epithelial cells to artificial materials including those of implants and hospital equipment (6–9). WTA also interacts with bacteriophages, enabling phage-dependent horizontal gene transfer of mobile genetic elements that govern virulence and antibiotic resistance of *Staphylococci* (10, 11). In addition, *Staphylococcus aureus* WTA has been shown to regulate the spatial and temporal localization of autolysin Atl (12) and penicillin-binding protein 4 (13, 14) essential to coordination of peptidoglycan hydrolysis and cross-linking, respectively. The absence of WTA reduces peptidoglycan cross-linking to a level that resensitizes methicillin-resistant *S. aureus* to certain β-lactam antibiotics. Together, these roles of WTA in virulence, antibiotic resistance, cell division, and peptidoglycan synthesis point to its biogenesis as a potential therapeutic target against infections caused by Gram-positive bacteria and β-lactam-resistant variants.

S. aureus WTA is synthesized by teichoic acid ribitol (Tar) enzymes in the cytosol on the membrane anchored carrier, undecaprenyl-phosphate (C₅₅-P) (15). The saccharides, phosphate-N-acetylglucosamine (P-GlcNAc) and N-acetylmannosamine (ManNAc), are first attached

to the phosphate headgroup of C₅₅-P through the consecutive actions of TarO (16) and TarA (17) to produce lipid β [ManNAc-β-(1-4)-GlcNAc-P-P-C₅₅]. Next, a series of polyol-phosphate glycosyltransferases (GTs), TarB, TarF, TarL, and TarK, attach two sn-glycerol-3-phosphate (GroP) moieties followed by a chain of D-ribitol-5-phosphate (RboP) (18, 19). The resulting lipid-linked WTA intermediate, RboP₄₀₋₆₀-GroP₂-ManNAc-β-(1-4)-GlcNAc-P-P-C₅₅, is known as lipid φ.40-60. Synthesis of lipid φ.40-60 is followed by intracellular glycosylation of the ribitol hydroxyl groups, by TarM (20), TarS (13), and/or TarP (21), before the export of the polar headgroup across the lipid bilayer by the ABC transporter, TarGH (22). On the extracellular surface, the ribitol hydroxyl groups are further modified by D-alanylation through the activities of DltA-D (23). The last step of WTA biogenesis involves the covalent transfer of WTA from C₅₅-P to peptidoglycan by LytR-CpsA-Psr (LCP) enzymes (24, 25). C₅₅-P is recycled and flipped across the membrane for either another round of WTA synthesis or for peptidoglycan synthesis. The importance of recycling C₅₅-P is demonstrated by the lethality of accumulating nonfunctional lipid-bound WTA intermediates in the absence of the polyol-phosphate GTs and the WTA transporter (26, 27).

The polyol-phosphate GTs in WTA biogenesis belong to the TagF-like family of monotopic membrane proteins with variants involved in the synthesis of other bacterial phosphosugar cell wall polymers such as capsular polysaccharide, O-antigen, and polyribosylribitol phosphate capsule (28–31). The WTA polymer building blocks, GroP and RboP, are derived from the donor substrates cytidine diphosphate (CDP)-glycerol and CDP-ribitol, respectively. TarB and TarF act sequentially on lipid β [ManNAc-β-(1-4)-GlcNAc-P-P-C₅₅] by each catalyzing the addition of a single GroP molecule (19). These reactions produce lipid φ.2 [GroP₂-ManNAc-β-(1-4)-GlcNAc-P-P-C₅₅] for RboP polymerization by either TarL or TarK, paralogs that arose from a gene duplication event of the *tarJL* locus (Fig. 1A) (19). The membrane-binding properties of these polymerases were first noted as their enzymatic activities were displayed using

¹Department of Biochemistry and Molecular Biology, The University of British Columbia, Vancouver, British Columbia, Canada. ²Centre for Blood Research, The University of British Columbia, Vancouver, British Columbia, Canada. ³Department of Biochemistry and Biomedical Sciences, Michael G. DeGroote Institute for Infectious Disease Research, McMaster University, Hamilton, Ontario, Canada.

*Corresponding author. Email: ncjs@mail.ubc.ca

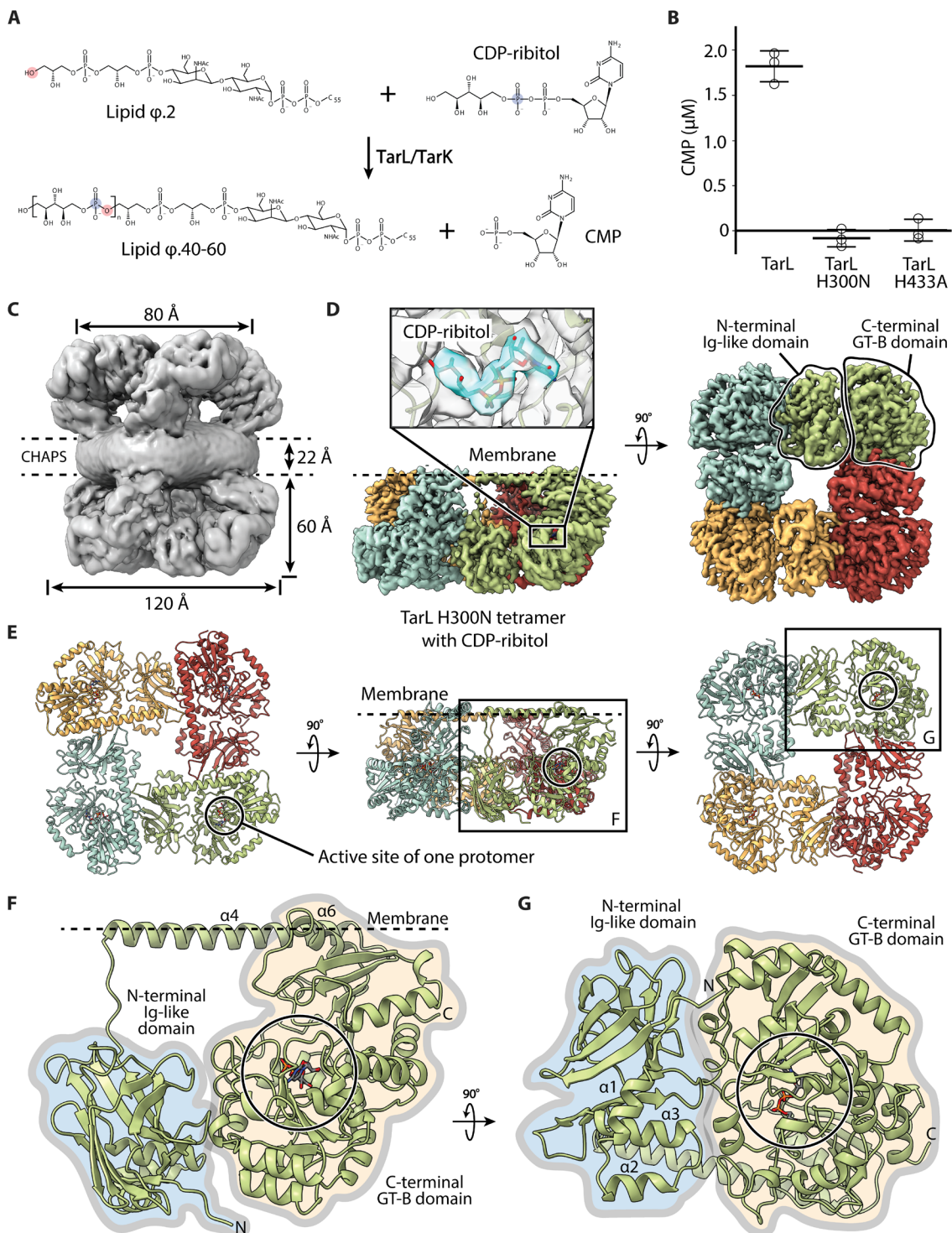


Fig. 1. Cryo-EM structure of *S. aureus* TarL H300N catalytic mutant in complex with CDP-ribitol. (A) TarL and TarK catalyze the polymerization of RboP on lipid φ.2 using CDP-ribitol as their donor substrate. The putative nucleophile and electrophile are highlighted in red and blue, respectively. (B) Phosphotransferase activity of TarL, TarL H300N, and TarL H433A was assessed by quantifying CMP released from 25 μM CDP-ribitol in the presence of heat-treated *S. aureus* RN4220 membranes providing the lipid acceptors. (C) Unsharpened cryo-EM map of TarL H300N with a micellar layer of CHAPS at 3.7-Å resolution (D4 symmetry applied). (D) Cryo-EM map of a TarL H300N tetramer at 3.4-Å resolution. Chains A, B, C, and D colored green, blue, orange, and red, respectively. EM map features at the active site of chain A are shown with CDP-ribitol depicted as sticks. Heteroatoms are colored by type (O, red; P, orange; N, blue). (E) Ribbon structure of the TarL H300N tetramer. (F) Side view of a TarL H300N protomer. (G) Bottom view of a TarL H300N protomer.

isolated membranes (18, 32, 33). *tarK* is nonessential; however, the dispensability of *tarL* remains unclear. One study showed that either *tarL* or *tarK* can be deleted but not both (34). Another study confirmed that *tarK* is dispensable; however, the authors reported the inability to knock out *tarL* unless *tarK* is overexpressed (35). Despite these uncertainties, WTA polymerization remains essential, and inhibitory compounds targeting TarL and TarK may additionally inactivate TarB and TarF, thereby halting WTA biosynthesis at multiple stages.

Divergence in WTA biosynthesis among different Gram-positive bacterial species mostly occurs at the stage of polyol-phosphate polymerization (fig. S1). Notably, WTA of *Staphylococcus epidermidis* is composed of a GroP chain, and its synthesis is catalyzed by a set of teichoic acid glycerol (Tag) enzymes. The addition of a single GroP group to lipid β (catalyzed by TagB) is sufficient to prime the WTA intermediate for GroP polymerization by TagF (36). A series of *S. epidermidis* TagF C-terminal domain (CTD; residues 312 to 721) crystal structures provide the only current structural understanding of the TagF-like family of enzymes (29). These structures revealed a glycosyltransferase-B (GT-B) domain (29, 37) with insertions of basic residues proposed to be involved in dimerization, stabilization of membrane-binding helices, and expansion of the active site cleft, presumably to bind the growing GroP polymer (29). Structures of TagF CTD in complex with CDP-glycerol support an S_N2 -like reaction involving the deprotonation of the terminal hydroxyl group of the polyol chain by an invariant histidine (H444) for nucleophilic attack on the β -phosphorus of CDP-glycerol (29). All TagF-like enzymes are predicted to have a membrane-binding GT-B domain, and members that act as polymerases have an additional and as yet largely uncharacterized domain at the N terminus that is not predicted to adopt a single, consistent fold among the various species.

Here, we present the cryo-electron microscopy (cryo-EM) structure of full-length, tetrameric *S. aureus* TarL H300N in complex with CDP-ribitol. In addition, we have elucidated crystal structures of the N-terminal domains of *S. aureus* TarL and TarK. Our work provides the structural basis underlying the atypical properties of TarL in membrane binding and in catalyzing ribitol-phosphate polymerization as a GT-B enzyme. We describe the selective binding of CDP-ribitol and the positioning of catalytic residues to provide mechanistic insights into ribitol-phosphate transfer. In addition, we propose a potential binding site for the electronegative acceptor lipid $\varphi.2$ based on the location of the active site and the clustering of basic residues. Furthermore, we propose that membrane-binding helices and an immunoglobulin (Ig)-like domain are used to position the GT-B domain for selecting lipid $\varphi.2$ over shorter WTA intermediates. Retention of the acceptor for polymerization is proposed to rely on clusters of basic residues that are ideally positioned to associate with the pyrophosphate group at the base of lipid $\varphi.2$ and the phosphate groups of the ribitol-phosphate polymer. The structural insights provided by our study contribute to our understanding of not only WTA biogenesis but also the biogenesis of other glycoconjugates that rely on the use of TagF-like enzymes.

RESULTS

Overall architecture of TarL

Single-particle cryo-EM analysis was performed using *S. aureus* TarL H300N purified with the zwitterionic detergent CHAPS and incubated

with the donor substrate CDP-ribitol (table S1 and fig. S2). The H300N mutation inactivates the putative function of H300 as the catalytic base and allows CDP-ribitol to remain intact in the active site for structural analysis (Fig. 1B). Three-dimensional (3D) reconstruction of protein particles remarkably revealed the presence of two TarL tetramers separated ~22 Å by an intervening micellar layer of CHAPS (Fig. 1C). The overall complex at 3.7-Å resolution was refined with D4 symmetry applied (Fig. 1C, fig. S2, and table S1). The relative position of the two tetramers (each ~120 Å by 120 Å by 60 Å in dimensions) is, however, not constrained, and symmetry expansion coupled with further 3D classification and local refinement led to the reconstruction of a 3.4-Å-resolution map of a single tetramer (Fig. 1, D and E; fig. S2; and table S1). The unambiguous boundary between TarL and the detergent micelle outlines the membrane-binding interface of TarL and is composed of two helices ($\alpha 4$ and $\alpha 6$) extending from each protomer (Fig. 1, C to F). This interface stretches across each tetrameric assembly, suggesting that the tetramer associates with the inner leaflet of the lipid bilayer as a stable biological unit. Oligomerization is a common strategy used by monotopic membrane proteins to increase their membrane-binding surface area through multivalent interaction, thereby strengthening membrane association (38). Each TarL protomer is composed of an N-terminal Ig-like domain (NTD; residues 1 to 163) and a C-terminal GT-B domain (CTD; residues 206 to 562) bound by CDP-ribitol (Fig. 1, D to G, and figs. S3 and S4). The NTD and CTD are connected through a near fully extended, remarkably structured coil (residues 164 to 170) and a 35-residue-long amphipathic helix ($\alpha 4$; residues 171 to 205).

The N-terminal Ig-like fold features two β sheets that pack face-to-face to form a sandwich-like structure (Fig. 1, F and G, and fig. S3). Proteins that adopt the Ig-like fold exhibit a diverse range of functions and variable insertions between its β strands (39). Notably, the TarL NTD has an insertion that forms three α helices ($\alpha 1$ to $\alpha 3$) between $\beta 8$ and $\beta 9$, and these helices are positioned at the center of the TarL tetramer (Fig. 1, E and G). The NTD is attached to amphipathic helix $\alpha 4$, which TarL uses to associate with the CHAPS micelle along with amphipathic helix $\alpha 6$ of the C-terminal GT-B domain (Fig. 1F). The GT-B domain of TarL is the putative RboP transferase domain with a tandem of Rossmann-type $\beta\alpha\beta$ folds. The more N-terminal subdomain has a nonclassical 213456 topology (denoting the order of the hydrogen-bonded β strands) parallel β sheet, whereas the more C-terminal subdomain adopts the classical Rossmann-type fold with a 321456 parallel β sheet (Fig. 1, F and G, and fig. S3). The two GT-B subdomains are separated by a deep solvent-exposed active site cleft that appears well suited for substrate binding and release of extended polymerized products. GT-B domain flexibility is observed. In opposing chains A and C (colored green and orange, respectively), the C-terminal subdomain is positioned closer to the N-terminal subdomain, constricting the cleft around the more clearly resolved CDP-ribitol bound in the active site (Fig. 1D and figs. S4 and S5). In chains B and D (colored blue and red, respectively), the cleft is more open with the CDP-ribitol less resolved but still clearly bound. Open-closed transitions of the GT-B subdomains are linked to catalytic competency (40), and here outlines a possible route of allostery linking the neighboring active sites via the NTD. The GT-B domain of TarL is reminiscent in overall architecture to the *S. epidermidis* TagF CTD (29), albeit with the observed interesting variations between the two species in oligomerization and membrane association [root mean square deviation (RMSD) of ~8 Å for 356 C α pairs; Protein Data Bank (PDB) ID: 3L7K chain D] (fig. S6).

NTDs of TarL and TarK

The NTD is central to TarL tetramerization. It forms an interaction interface with the CTD of the adjacent protomer (Fig. 2A) with an interface area of 900 to 930 Å² stretching across both β sheets of the NTD with the complementary site on the CTD formed by the extended regions between β15 and β16 as well as β16 and β17. In addition, the NTD forms extensive intrachain interactions with the CTD of the same protomer, with an additional interface area of 560 to 660 Å² encompassing β8, and the loops between β3 and β4 as well as β10 and β11 (Fig. 2A). These features pack against α13–α14, α18, and their preceding loops that are oriented differently between the two observed GT-B conformational states (fig. S5). Despite the dynamic binding interface, this intraprotomer contact plays a critical architectural role in positioning the two domains for tetramerization.

Before structural determination of TarL by cryo-EM, we determined crystal structures of *S. aureus* TarL NTD (residues 1 to 169) and TarK NTD (residues 1 to 171) (65% sequence identity) to 1.7 Å (1 molecule in the asymmetric unit) and 3.0 Å (10 molecules in the asymmetric unit) resolution, respectively (table S2 and Fig. 2B). Superposition of our NTD crystal structures (chain A of TarL NTD with chains A to J of TarK NTD) revealed RMSD values of 2.3 to 2.7 Å for 133 Cα pairs. Furthermore, our TarL structures superimposed at the NTD display an RMSD value of ~2 Å for 156 Cα pairs. The structural differences observed at the NTDs are mainly associated with crystal packing (fig. S7B).

Monotopic membrane association features of TarL

The membrane boundary was predicted by the PPM 3.0 web server to intersect amphipathic helices α4 and α6 as well as the loop preceding α6 (Figs. 1F and 2A). α4 sits parallel to the membrane plane, whereas α6 dips into the membrane at its N terminus. Both helices have clusters of positively charged residues that are ideally positioned to form electrostatic interactions with negatively charged functional groups of the phospholipid headgroups (Fig. 2C). The neighboring residues at the predicted cytosol/membrane interface are predominantly nonpolar with an enrichment of aromatic amino acids that can both partition into the lipid bilayer and form cation-π interactions with lipid headgroups (41). Last, the nonpolar side of the interface features a variety of hydrophobic side chains that can extend into the hydrocarbon core of the lipid bilayer and pack against the acyl chains of lipids (Fig. 2D). This nonpolar region is estimated by the PPM 3.0 web server to extend ~6.2 Å into the membrane with ΔG_{transfer} (water-to-membrane transfer energy) of -74 kcal/mol.

Several extra features not attributable to TarL are observed in the map including notably at the predicted membrane interface between α4 and α6 (Fig. 2, A and C and fig. S8). This feature, present in all four protomers, spans across both polar and nonpolar regions of TarL, suggesting that the bound molecule is likely to be CHAPS. It is tempting to speculate that these outline a binding site for lipid φ.2 with the predicted polar region, surrounded by highly conserved basic residues, marking the area that occupies the negatively charged pyrophosphate group (Fig. 2C). Besides R191 on α4 and K262 on α6, the loop preceding α6 features K250, R256, and R257. In support of this, this region is ~23 Å away from the β-phosphorus of CDP-ribitol (putative electrophile), matching the approximate length of GroP₂-ManNAc-β-(1-4)-GlcNAc that extends from the pyrophosphate group of lipid φ.2 [GroP and the disaccharide are estimated to be ~6 and ~10 Å in length, respectively, based on various ligand-bound crystal structures (29, 42, 43)] (Fig. 3A).

C-terminal GT-B domain of TarL

On the basis of the structure here, the orientation of the TarL GT-B domain is rigidified by its interactions with the CHAPS micelle and neighboring NTDs (Fig. 2). These interactions are predicted to fix the position of the active site relative to the membrane, providing a structural basis for RboP polymerization on the terminal GroP of lipid φ.2 over that of lipid φ.1 estimated to be ~6 Å shorter (Fig. 3A). Between the micelle and the active site, a groove is ideally positioned to bind the headgroup of lipid φ.2. It is in contact with the amphipathic molecule (presumably CHAPS) that sits at the proposed membrane interface in our structure, and it features the region between β14 and β15 (residues 278 to 286) with two aromatic residues (F280 and Y285) that are often observed in binding of carbohydrate substrates. The equivalent groove has previously been proposed to be an acceptor binding site of various membrane-associated GT-B enzymes (40, 44, 45). Away from the proposed membrane-binding features, the surface of TarL is predominantly negatively charged with patches of basic residues that, we propose, are logically positioned around each active site to facilitate association with the phosphate groups of elongating WTA chains (Figs. 2E and 3B).

In studies on *Bacillus subtilis* 168 TagB (46), *B. subtilis* 168 TagF (46), and *S. epidermidis* TagF (29), two invariant histidine residues were shown to be critical for activity. On the basis of our cryo-EM structure, the most likely catalytic candidates of TarL are H300 and H433 with possible roles in activating the nucleophile and protonating the leaving group, respectively (29, 46). To probe this further, we quantified cytidine monophosphate (CMP) released by either wild-type TarL, TarL H300N, or TarL H433A in the presence of CDP-ribitol and heat-inactivated *S. aureus* membranes providing the lipid acceptor. The mutants displayed negligible activity compared to wild-type TarL, confirming the critical roles of H300 and H433 (Fig. 1B). In the active site of the TarL H300N cryo-EM structure, CDP-ribitol is oriented with its ribitol group bent back toward the cytidine moiety as observed with CDP-glycerol in the structures of *S. epidermidis* TagF CTD (29) and the corresponding groups of other donor substrates bound to membrane-associated GT-B enzymes such as PglH (44), PimA (47), and WaaG (48) (Fig. 3C). In contrast to these latter GT-B enzymes, TarL and TagF are predicted to catalyze nucleophilic attack on the β-phosphorus instead of the adjacent anomeric carbon of the sugar donor. This difference is reflected by the projection of the β-phosphate group of the donor, rather than the adjacent carbon of the polyol moiety, toward the membrane where the lipid-linked acceptor is located (Fig. 3A). In addition, the donor sugar binding sites of TarL and TagF are atypical of GT-B enzymes as they are formed by the loop extending from β15 of the more N-terminal GT-B Rossmann-like subdomain rather than features at the more C-terminal subdomain (Fig. 3D).

The cytidine moiety of the donor substrate is accommodated in a pocket outlined by loops and helices extending from β18 to β21 (Fig. 3C). P395 terminates hydrogen bonding between β18 and β19 to accommodate the N4 amine group of the cytidine moiety. The ribose moiety of the donor is positioned at a suitable distance for hydrogen bonding between one of its hydroxyl groups and the side chain of E497. In addition, the dipole of α17 is ideally positioned to neutralize the negative charge of the pyrophosphate group. In the observed closed state of the GT-B domain (chains A and C), the α-phosphate is within hydrogen bonding distance with the NE2 atom of the invariant histidine, H433 (Fig. 3C and figs. S4 and S5), supporting the proposed role of the histidine in protonating the

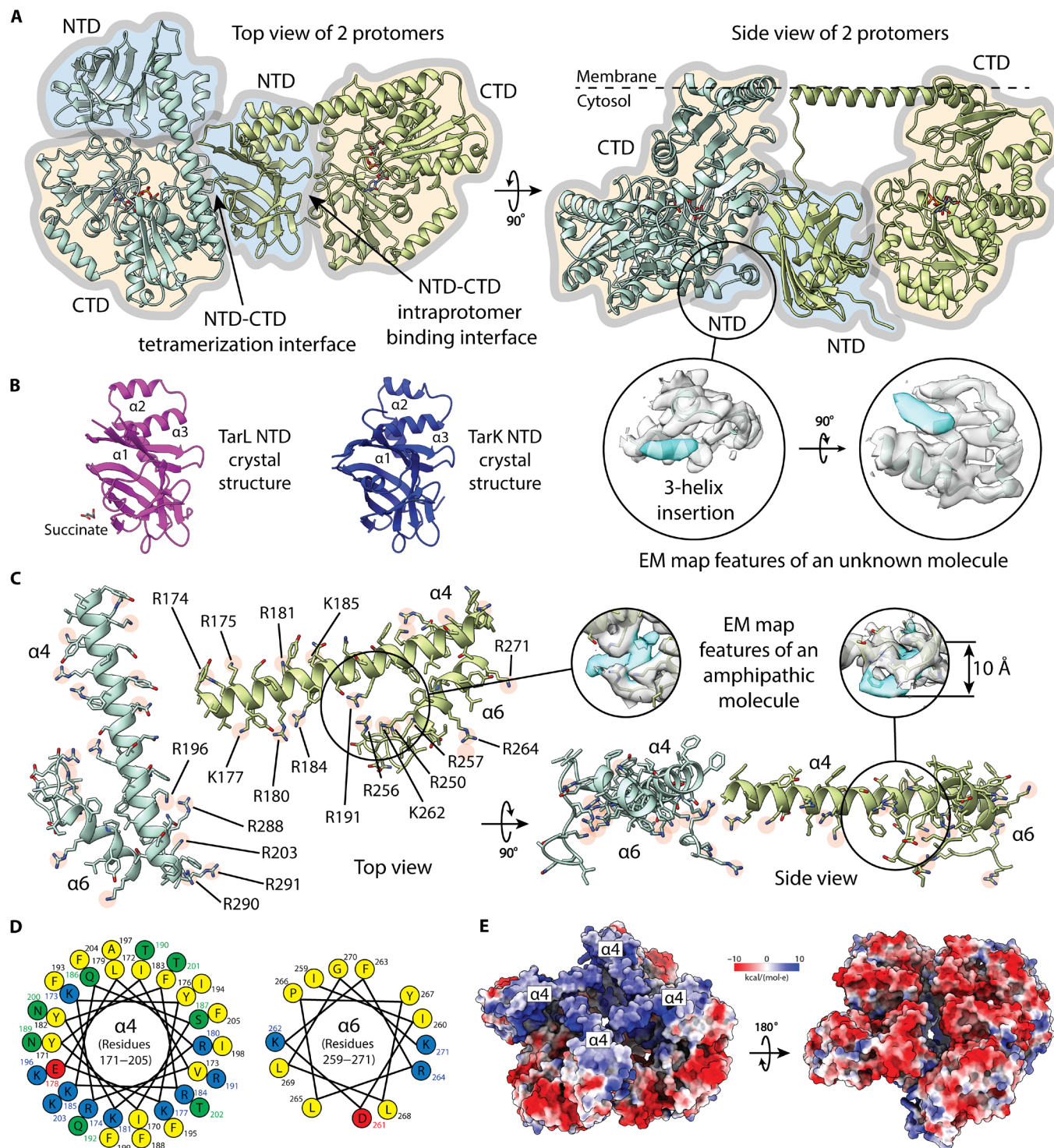


Fig. 2. NTD and amphipathic features of TarL. (A) Ribbon structures of chains A and B colored in green and blue, respectively. Inset depicts EM map features of an unknown molecule bound to the three-helix insertion of TarL NTD. (B) Crystal structures of TarL NTD and TarK NTD. (C) Amphipathic features of two TarL protomers. Hetero-atoms are colored by type (O, red; N, blue). The side chains of basic residues are highlighted in salmon. Inset depicts EM map features of an amphipathic molecule between $\alpha 4$ and $\alpha 6$. (D) Helical wheel diagrams of amphipathic helices $\alpha 4$ and $\alpha 6$ (basic residues, blue; acidic residues, red; uncharged polar residues, green; nonpolar residues, yellow). (E) Electrostatic surface potential of the TarL tetramer.

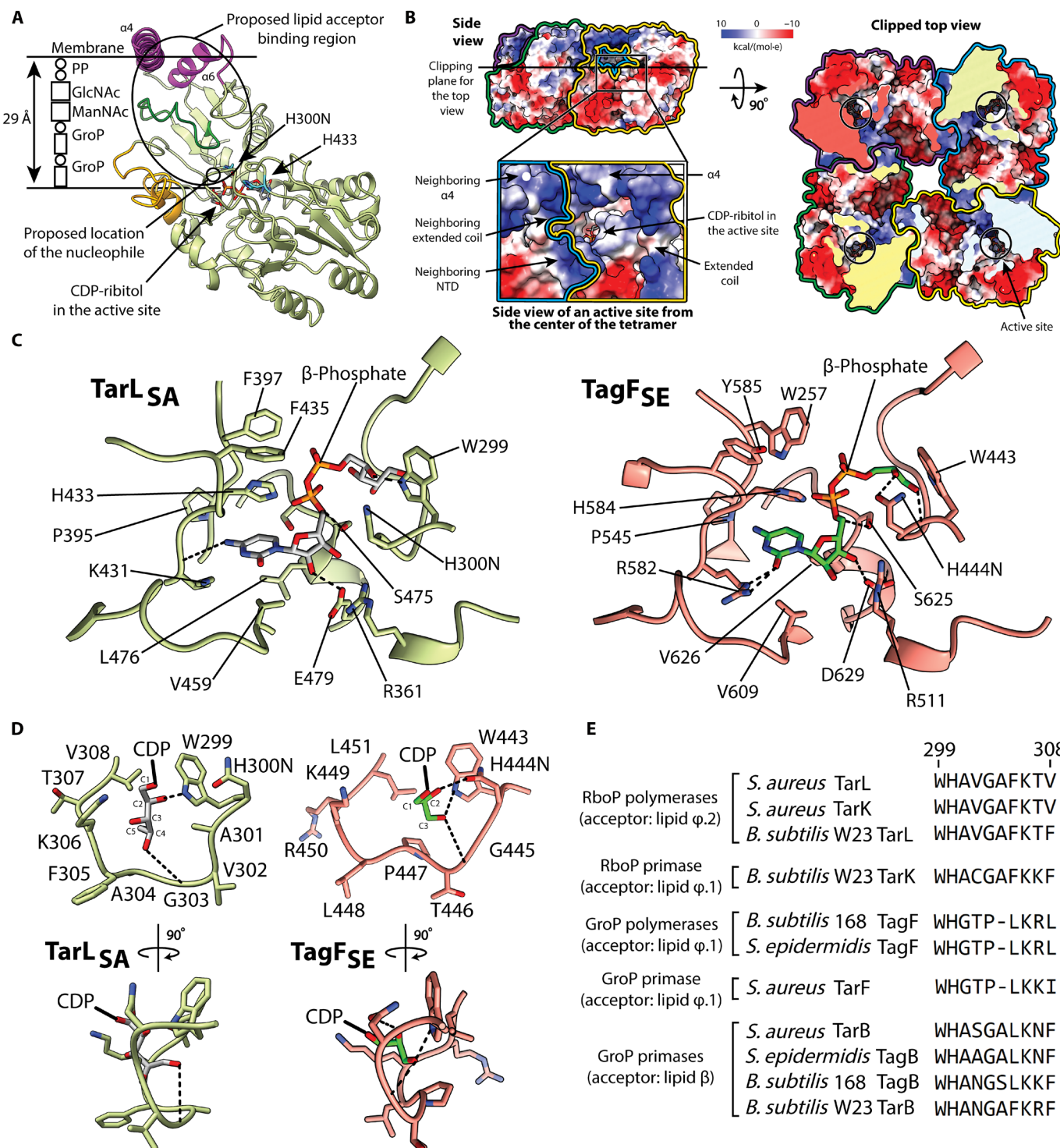


Fig. 3. C-terminal GT-B domain of TarL. (A) Ribbon structure of the CTD and amphipathic helices (purple) of a TarL protomer (chain A). The proposed acceptor-binding region and tetramerization site are shown in green and orange, respectively. H300N and H433 are shown in cyan and CDP-ribitol is shown in gray. Heteroatoms are colored by type (O, red; P, orange; N, blue). (B) Electrostatic surface potential around the active site of TarL (chain B). (C) Active sites of TarL (chain A) and *S. epidermidis* TagF (residues 312 to 721; PDB ID: 3L7K) with select residues depicted as sticks. CDP-ribitol and CDP-glycerol are shown in gray and green, respectively. (D) Structural features at the donor polyol-phosphate binding site of TarL (chain A) and *S. epidermidis* TagF. (E) Sequence alignment at the proposed donor polyol-phosphate binding site of select TagF-like enzymes.

α -phosphate group to facilitate CMP departure. Intriguingly, the loop with H433 (extending from β 19) is positioned away from the donor substrate in the more open state of the GT-B domain (chains B and D) that may be suitable for the exchange of CMP for CDP-ribitol (figs. S4 and S5). The opposing conformational states of neighboring GT-B domains outline a possible allosteric mechanism that coordinates the catalytic cycle between the four protomers; however, only subtle conformational differences are observed at the bridging Ig-like domains (fig. S5).

The donor ribitol-binding site of TarL is formed by the loop extending from β 15 (residues 299 to 308) (Fig. 3, C and D) with the carbon atoms of the ribitol group sandwiched by the nonpolar regions of A301 and K306. The side chain of the putative active site base, H300 (mutated to asparagine in the structure here), is expected to project into the active site cleft and π -stack with the indole side chain of W299 as observed with the corresponding residues in wild-type *S. epidermidis* TagF CTD (PDB ID: 3L7I) (29). This interaction is proposed to orient and stabilize the imidazole group for activating the nucleophile.

TarL selects for the ribitol group of CDP-ribitol over the glycerol group of CDP-glycerol using an enlarged polyol-binding site (Fig. 3, D and E). The ribitol-binding site of TarL features G303, A304, and F305 in place of P447 and L448 in the glycerol-binding site of TagF. G303 and A304 of TarL both enlarge the binding site and alleviate the steric clashes that would otherwise occur with the presence of a proline. In addition, the bulky side chain of TarL F305 packs against neighboring residues to fix the position of the expanded ribitol-binding loop. *S. aureus* TarK and *B. subtilis* W23 TarL and TarK are other characterized RboP transferases, and they all have the ribitol-binding GAF motif. Furthermore, the glycerol-binding PL motif is observed in the sequences of the GroP transferases, *B. subtilis* W23 TarK, *B. subtilis* 168 TagF, and *S. aureus* TarF (Fig. 3E). The proposed use of a GAF motif for ribitol binding and a PL motif for glycerol binding do not strictly apply to TarB/TagB GroP primases. *B. subtilis* 168 TagB has a GSL motif and both *S. aureus* TarB and *S. epidermidis* TagB have a GAL motif. Although these putative CDP-glycerol-binding enzymes have an expanded polyol-phosphate-binding region, they all lack the phenylalanine (TarL F305) that stabilizes the expanded conformation of the loop for ribitol binding. Intriguingly, *B. subtilis* W23 TarB has the proposed ribitol-binding GAF motif, suggesting that the enzyme may use CDP-ribitol as its donor substrate.

DISCUSSION

Monotopic membrane association features of WTA polymerases

Monotopic membrane proteins, which represent the least characterized general class of membrane proteins at the atomic level [\sim 0.06% of non-redundant structures reported (38)], play a central role in catalyzing reactions on lipid-bound substrates. Our structure of *S. aureus* TarL is one of the first cryo-EM structures of a monotopic membrane protein, expanding our insight into this important class of proteins and, in particular, membrane-associated GT-B enzymes. Similar to many other monotopic proteins, TarL associates with the membrane through amphipathic helices and oligomerizes to increase its membrane-binding surface area and stability via repeating multivalent interactions (38). However, these features of TarL are elaborate as helix α 4 is considerably longer than other monotopic helices that have been described, and the oligomeric state of TarL is higher than most monotopic proteins

(38). Intriguingly, *S. aureus* TarL and its *S. epidermidis* counterpart, TagF, are observed to use distinct membrane-binding features, highlighting the variability used by monotopic GT-B enzymes to associate with the membrane and position their active sites to bind specific lipid-linked acceptor substrates (fig. S9). The sole membrane-binding feature observed in the structure of TagF CTD is a two- α -helix region that corresponds to α 4 of TarL (fig. S6). The break between the two helices appears to be induced by a group of three positively charged residues (RRK). In addition, the TagF helix corresponding to α 6 of TarL is not amphipathic, and the preceding region forms a β strand as typically observed with GT-B enzymes. Furthermore, the two- α -helix region along with the aforementioned CTD region encompassing residues 452 to 481 of TagF was found to mediate dimerization in crystal structures of TagF CTD (fig. S6A). These structural differences at the putative membrane-binding regions implicate alternate mechanisms of acceptor substrate binding. TagF catalyzes GroP polymerization on lipid φ .1, whereas TarL catalyzes RboP polymerization on the longer lipid φ .2.

Proposed catalytic mechanism of TarL in WTA polymerization

Our structural and biochemical data suggest that H300 initiates RboP polymerization by deprotonating the C3 hydroxyl group of the terminal GroP of lipid φ .2 for nucleophilic attack on the β -phosphorus of CDP-ribitol (Fig. 4). The indole ring of W299 is ideally positioned to stabilize the protonated imidazole group of H300 through a cation- π interaction (Fig. 3C). Furthermore, we propose that the nucleophilic oxygen aligns with both phosphorus groups of the donor for an in-line attack as observed with biological phosphoryl-transfer reactions (49). The imidazole side chain of H433, in contact with the α -phosphate group of CDP-ribitol (in chains A and C), may stabilize the resulting pentacoordinate transition state and facilitate the departure of the CMP leaving group by donating a proton. The dipole of α 17 may also facilitate the departure of CMP by stabilizing the developing negative charge. The following exchange of CMP with CDP-ribitol may be promoted by the observed open state of the GT-B domains in chains B and D of the tetramer (fig. S5). Subsequent rounds of RboP attachment to the lipid substrate then continues with the initial step involving the deprotonation of the C5 hydroxyl group of the terminal RboP of lipid φ .3 (Fig. 4). Intriguingly, the catalytic cycles may be coordinated between the four protomers as neighboring GT-B domains, linked by the Ig-like domains, adopt opposite conformational states (fig. S5). As the RboP chain is lengthened, the base of the lipid-linked acceptor may become free to occupy more distant binding sites similar to the molecular ruler mechanism proposed for bacterial GT PglH (44), where the pyrophosphate group of a lipid-linked oligosaccharide acceptor binds a “ruler” helix and is successively positioned further from the active site on substrate addition. In this scenario for TarL, the clusters of basic residues lining the proposed membrane interface are all potential points of contact with the pyrophosphate group (Fig. 2C). Our proposed S_N2 -like catalytic mechanism aligns with the conventional single-displacement mechanism proposed for inverting GTs, except that the nucleophile attacks a phosphorus center rather than a carbon center (50). This results in the breaking of a pyrophosphate bond instead of a carbon-oxygen bond of a closed-ring sugar. The clusters of basic residues surrounding each active site of TarL suggest that they are positioned to facilitate polymerization by retaining the growing phosphate-rich polymer within the tetramer until \sim 40 to 60 RboP units are transferred

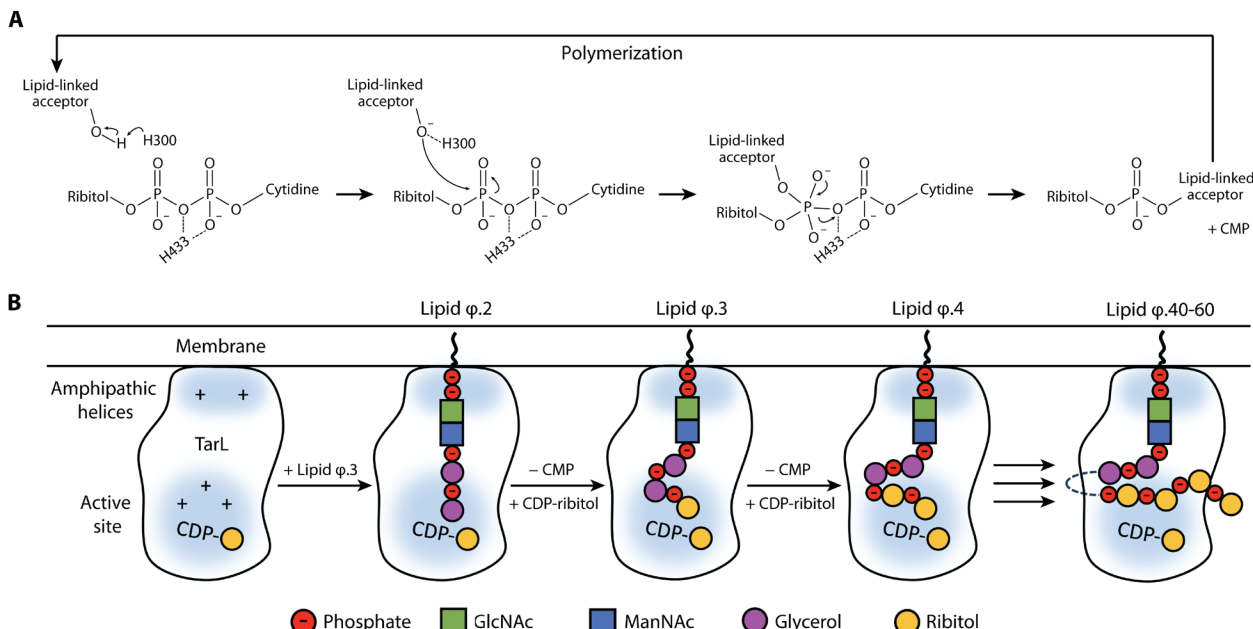


Fig. 4. WTA polymerization by TarL. (A) Proposed mechanism of ribitol-phosphate polymerization on lipid φ.2 by TarL. (B) Schematic representation of TarL-mediated WTA polymerization. The architecture of the TarL tetramer shows that the position of the active site is largely fixed relative to the surface of the CHAPS micelle (presumably marking the membrane interface), providing a structural basis for ribitol-phosphate polymerization on the terminal glycerol-phosphate of lipid φ.2 over that of lipid φ.1 estimated to be ~6 Å shorter. The large clusters of electropositive residues (highlighted in blue) at the amphipathic helices and active site are ideally positioned to retain the electronegative lipid-linked acceptor for polymerization. Polymerization likely terminates through limiting steric and electrostatic factors coupled with restrictions of membrane binding that orient the terminus of the growing polymer away from the catalytic center.

(Fig. 3B). As suggested for *S. epidermidis* TagF, polymerization likely terminates through limiting steric and electrostatic factors coupled with restrictions of membrane binding that orient the terminus of the growing polymer away from the catalytic center (29).

Regulation of product chain length by *S. aureus* WTA polymerases

The reported differences in the lengths of polyol-phosphate polymers produced by WTA polymerases in vitro appear to be associated with differences in the localization of the acceptor substrate. GroP chains polymerized by *B. subtilis* 168 TagF in a detergent-free environment on a soluble acceptor analog ($\text{C}_{13}\text{PP-GlcNAc-ManNAc-GroP}$) were found to vary in length depending on the ratio of donor to acceptor, indicating a distributive mechanism of polymerization (36). In a similar assay conducted with protease-treated *B. subtilis* membranes, TagF catalyzed the formation of GroP chains of physiological length on presumably lipid φ.1 (51, 52). These findings suggest that the membrane and intrinsic properties of the polymerase are involved in regulating polymer length. As our cryo-EM study revealed that TarL solubilized in CHAPS forms protein-detergent-protein assemblies, we speculate that the CHAPS micelle can functionally mimic the biological membrane and thus regulate polymerization on lipid-linked acceptors. In vitro activity assays conducted with CDP-ribitol, a farnesyl-bound acceptor analog ($\text{C}_{15}\text{PP-GlcNAc-ManNAc-GroP}_2$), and *S. aureus* TarL extracted from the membrane with CHAPS led to the formation of polymers with defined lengths; however, these polymers were estimated to be 10 RboP units shorter than those extracted from *S. aureus* (19). Furthermore, processive characteristics were noted as polymer lengths remained similar when substrate ratios or enzyme concentrations were varied (experimental results were not shown) (19). These results

obtained with *S. aureus* TarL are compatible with the notion that CHAPS micelles can mimic membranes and regulate polymerization. The production of shorter polymers may be associated with poor mobility of the lipid-linked acceptor within CHAPS micelles. Collectively, the results of these in vitro assays reveal a membrane-dependent regulatory mechanism that is used by WTA polymerases to terminate chain elongation at specific lengths.

Structural organization of WTA polymerases and other TagF-like enzymes

WTA polymerases and WTA modifying GTs are functionally related enzymes that appear to have evolved into species-specific variants through domain duplication and shuffling. In contrast to the Ig-like NTD of *S. aureus* WTA polymerases, the NTD of *S. epidermidis* TagF is predicted to adopt a GT-A fold that resembles the catalytic domain of *S. aureus* TarS and TarP, GTs that attach β-O-GlcNAc to the ribitol moieties of WTA (fig. S6D). This predicted fusion of the two GT domains implicates concurrent WTA polymerization and modification in *S. epidermidis*. Another example of the acquisition and functional specialization of homologous domains between WTA polymerases and WTA modifying GTs is observed in the structural homology between the Ig-like NTD of TarL and the “C1” trimerization domain of TarS (53) (residues 353 to 495; PDB ID: 5U02) found by the DALI sever (54) (RMSD of 7.1 Å over 129 Cα pairs) (fig. S7C).

S. aureus TarB, TarF, TarL, and TarK are all TagF-like enzymes with sequences aligning at the GT-B domain (fig. S10). As both upstream GroP primases, TarB and TarF, lack a domain preceding the membrane-binding region, the orientation of their GT-B domains is expected to be less restrained and thus allows for their use of shorter WTA intermediates as acceptor substrates. Furthermore,

these GroP primases may use specific features to bind the different terminal moieties of their unique acceptors (i.e., the binding of the ManNAc moiety of lipid β and the GroP-ManNAc moiety of lipid φ .1 by TarB and TarF, respectively).

TagF-like enzymes have also been identified outside of WTA synthesis, and these enzymes are involved in the production of bacterial phosphosugar cell wall polymers such as capsular polysaccharide (28–31) (e.g., *Streptococcus pneumoniae* serotype 23F gene product cps23FK and TagF-like capsule polymerases Cps3D, Cps7D, Cps1B, Ccs2, CslB, and Cps12B), O-antigen (29) (e.g., *Escherichia coli* WbeS), and polyribosylribitol phosphate capsule (29) (e.g., *Haemophilus influenzae* Q48156). Notably, the TagF-like capsule polymerases were found to catalyze the synthesis of complex polymers by combining their activities with other conjugated GTs (31). Furthermore, some of the TagF-like GT-B domains of the capsule polymerases were found to catalyze the transfer of hexose-phosphate rather than polyol-phosphate (31). The involvement of TagF-like enzymes in the production of multiple unique cell wall polymers of both Gram-positive and Gram-negative bacteria show that TagF-like enzymes are highly versatile and widely utilized GTs.

MATERIALS AND METHODS

Cloning, expression, and purification

DNA sequence encoding for full-length *S. aureus* TarL was amplified by polymerase chain reaction and cloned into a pET41b (Novagen) vector for expression with a thrombin-cleavable hexahistidine tag. *E. coli* BL21 (DE3) transformed with the plasmids were grown at 37°C until OD₆₀₀ (optical density at 600 nm) reached 0.6 in 2× YT media supplemented with kanamycin (50 μ g/ml) (table S3). Isopropyl- β -D-thiogalactopyranoside (0.5 mM) was then added to induce expression of the target proteins, and the temperature was lowered to 16°C for 18 hours. Cells were harvested by centrifugation and resuspended in 20 mM Hepes (pH 8), 500 mM NaCl, 16 mM CHAPS, and 25 mM imidazole for lysis using an Avestin EmulsiFlex-C5 homogenizer. Cell debris was pelleted by centrifugation at 125,000g for 45 min, and the supernatant was loaded on a 1-ml HisTrap FF column (GE Healthcare Life Sciences) equilibrated in the lysis buffer. The column was washed with 25 column volumes of 20 mM Hepes (pH 8), 500 mM NaCl, 6.5 mM CHAPS, and 25 mM imidazole before elution with a linear imidazole gradient up to 500 mM in 25 ml. Purified enzymes were concentrated with an Amicon Ultra centrifugal filter (100 kDa MWCO; EMD Millipore) and incubated with thrombin overnight at 4°C. Untagged proteins were further purified by size exclusion chromatography with a Superose 6 Increase 10/300 GL column (GE Healthcare Life Sciences) equilibrated with 20 mM Hepes (pH 7.5), 500 mM NaCl, and 6.5 mM CHAPS. TarL mutants (H300N and H433A) were made using the QuikChange mutagenesis kit (Strategene) and purified using the protocol outlined above.

Cloning, protein expression, and purification of *S. aureus* TarL NTD (residues 1 to 169) and TarK NTD (residues 1 to 171) were performed as outlined above with the following changes (table S3). Resuspension of cell pellets and purification were performed without CHAPS. Furthermore, size exclusion chromatography was performed using a Superdex 75 10/300 GL column (GE Healthcare Life Sciences) equilibrated with 20 mM Hepes (pH 8), 300 mM NaCl for TarL NTD and 25 mM Hepes (pH 8), 150 mM NaCl, and 3 mM TCEP for TarK NTD. Peak fractions were pooled and concentrated to ~25 mg/ml with a 10-kDa Amicon Ultra centrifugal filter (EMD Millipore).

TarL activity assays

The phosphotransferase activity of TarL, TarL H300N, and TarL H433A was assessed in triplicate with an end-point luminescence assay based on the release of CMP. The donor substrate CDP-ribitol was synthesized as previously described (55). The lipid acceptor substrate was provided by membranes isolated from *S. aureus*. Briefly, *S. aureus* RN4220 was cultured overnight at 37°C in tryptic soy broth. Harvested cells were lysed in 20 mM Hepes (pH 7.5) and 500 mM NaCl using a cell disrupter system (Constant Systems Ltd) at 40,000 p.s.i. Cell debris was pelleted at 12,000g for 30 min, and the supernatant was collected for another round of centrifugation at 125,000g for 45 min. The membrane pellet was resuspended in 20 mM Hepes (pH 7.5) and 150 mM NaCl. Proteins isolated with the membrane were inactivated by incubation at 65°C for 30 min. Reaction solutions were prepared in 20 mM Hepes (pH 7.5), 150 mM NaCl, 0.1% CHAPS with 25 μ M CDP-ribitol, and 1 μ M of TarL, TarL H300N, or TarL H433A. These reaction mixtures were incubated at 37°C for 1 hour before CMP was quantified using the UMP/CMP-glo GT (Promega) assay kit according to the manufacturer's instructions. The luminescence of 20- μ l aliquots was measured with a Synergy H4 multimode plate reader (BioTek). Readings were taken every minute for 10 min to ensure that luciferase reactions were complete. Background luminescence was determined with reactions containing heat-inactivated TarL, TarL H300N, or TarL H433A.

Cryo-EM sample preparation and data collection

For cryo-EM analysis, 3 μ l of TarL H300N (9.3 mg/ml) with 5 mM CDP-ribitol in 20 mM Hepes (pH 7.5), 500 mM NaCl, and 6.5 mM CHAPS was applied to a glow-discharged Lacey carbon 300 mesh grid (Ted Pella, 01895-F), blotted for 1.5 s at 100% humidity, and plunge-frozen into liquid ethane using a Vitrobot Mark IV (Thermo Fisher Scientific). Grids were screened at the High-Resolution Macromolecular Cryo-electron Microscopy (HRMCM) facility (Vancouver, British Columbia, Canada) on a 200-kV Glacios microscope (Thermo Fisher Scientific) equipped with a Falcon III camera (Thermo Fisher Scientific). A total of 19,380 movies were collected at the Pacific Northwest Center for Cryo-EM (PNCC; Portland, Oregon, USA) on a 300-kV Titan Krios (Thermo Fisher Scientific) equipped with a K3 camera (Gatan). Data were collected in super-resolution counting mode with 0.5295 Å per super-resolution pixel (1.059 Å per physical pixel; calibrated magnification of 81,000 \times). Each movie was collected with a total dose of 50 electrons/Å² fractionated across 50 frames. Automated data collection was carried out using SerialEM with a nominal defocus range set from -1 to -2.5 μm.

Cryo-EM data processing and model building

Initial processing was performed with RELION-3.1. The 19,380 movies were motion-corrected using MotionCor2 to generate summed and dose-weighted micrographs binned to 1.059 Å per pixel. The contrast transfer functions of these micrographs were determined using CT-FFIND4. Particles were auto-picked using the Laplacian-of-Gaussian-based method from a subset of micrographs to generate reference-free 2D-class averages. The best class averages were used as templates for particle picking with all micrographs. A total of 7.4 million particles were picked for initial processing. Reference-free 2D classification followed by initial de novo 3D model generation and 3D classification were performed with RELION-3.1 to remove junk and ice particles as well as particles picked from the carbon film. A total of 3.7 million particles were imported into cryoSPARC for additional rounds of

3D classification. A total of 1.3 million particles generating reconstructions with approximate D4 symmetry were selected and used for nonuniform refinement (with D4 symmetry) to generate a 3.7-Å-resolution map of the overall complex. Symmetry expansion using D4 symmetry coupled with further 3D classification and local refinement of a masked tetramer led to the reconstruction of a 3.4-Å-resolution map (without symmetry imposed) using 190,753 particles. The crystal structure of TarL NTD and a homology model of TarL CTD [built with Rosetta (56) using a structure of TagF CTD as template] were docked into the cryo-EM map for each TarL protomer using UCSF Chimera (57). The tetrameric structure was refined using Phenix (58) and Coot (59).

Crystallization and structure determination

TarL NTD (20 mg/ml) was crystallized at room temperature in 0.8 M succinic acid (pH 7) using the sitting drop vapor diffusion method. The crystals were cryoprotected in mother liquor supplemented with 30% glycerol and flash-cooled in liquid nitrogen. Hg²⁺-bound TarL NTD crystals were prepared by soaking TarL NTD crystals for 2 min in mother liquor supplemented with ~40 mM ethylmercury chloride. TarK NTD (24 mg/ml) was crystallized at room temperature in 0.1 M tris (pH 8.5), 100 mM NaCl, 75 mM MgCl₂, and 33% PEG-400 (polyethylene glycol, molecular weight 400) using the sitting drop vapor diffusion method. The crystals were cryoprotected in mother liquor supplemented with 25% glycerol and flash-cooled in liquid nitrogen. Diffraction data were collected with the 08ID-1 beamline of the Canadian Light Source (CLS; Saskatoon, Saskatchewan, Canada), the 23-ID-B beamline of the Advanced Photon Source (APS; Lemont, Illinois, USA), and the 5.0.2 beamline of the Advanced Light Source (ALS; Berkeley, California, USA). Datasets were processed with either XDS (at APS and ALS) (60) or Autoprocess (at CLS) (61). The structure of Hg²⁺-bound TarL NTD was determined by single-wavelength anomalous diffraction phasing using Phenix AutoSol (58, 62) with data collected (at APS) at the 1.0-Å peak wavelength. The structures of native TarL NTD (data collected at CLS) and TarK NTD (data collected at ALS) were solved by molecular replacement using the structure of Hg²⁺-bound TarL NTD (all atoms of chain A) as the starting model in Phaser-MR (62). Model building and refinement were performed with Phenix and Coot (59, 63).

Analysis software

Structures were visualized and represented using UCSF ChimeraX (64). Interactions were probed using LigPlot (65). Sequence alignments were produced using the ESPript 3.0 server (66). Helical wheel diagrams were generated using NetWheels (67). The positioning of proteins in membranes was predicted using the PPM Web Server (68).

Supplementary Materials

This PDF file includes:

Figs. S1 to S10

Tables S1 to S3

REFERENCES AND NOTES

- A. Bera, R. Biswas, S. Herbert, E. Kulauzovic, C. Weidenmaier, A. Peschel, F. Götz, Influence of wall teichoic acid on lysozyme resistance in *Staphylococcus aureus*. *J. Bacteriol.* **189**, 280–283 (2007).
- X. Wu, J. Zha, M. A. G. Koffas, J. S. Dordick, Reducing *Staphylococcus aureus* resistance to lysostaphin using CRISPR-dCas9. *Bioeng.* **116**, 3149–3159 (2019).
- T. Kohler, C. Weidenmaier, A. Peschel, Wall teichoic acid protects *Staphylococcus aureus* against antimicrobial fatty acids from human skin. *J. Bacteriol.* **191**, 4482–4484 (2009).
- D. Ulluwishewa, L. Wang, C. Pereira, S. Flynn, E. Cain, S. Stick, F. J. Reen, J. P. Ramsay, F. O'Gara, Dissecting the regulation of bile-induced biofilm formation in *Staphylococcus aureus*. *Microbiology* **162**, 1398–1406 (2016).
- J.-H. An, K. Kurokawa, D.-J. Jung, M.-J. Kim, C.-H. Kim, Y. Fujimoto, K. Fukase, K. M. Coggesshall, B. L. Lee, Human SAP is a novel peptidoglycan recognition protein that induces complement-independent phagocytosis of *Staphylococcus aureus*. *J. Immunol.* **191**, 3319–3327 (2013).
- V. Winstel, P. Kühner, F. Salomon, J. Larsen, R. Skov, W. Hoffmann, A. Peschel, C. Weidenmaier, Wall teichoic acid glycosylation governs *Staphylococcus aureus* nasal colonization. *mBio* **6**, e00632 (2015).
- C. Weidenmaier, J. F. Kokai-Kun, S. A. Kristian, T. Chanturiya, H. Kalbacher, M. Gross, G. Nicholson, B. Neumeister, J. J. Mond, A. Peschel, Role of teichoic acids in *Staphylococcus aureus* nasal colonization, a major risk factor in nosocomial infections. *Nat. Med.* **10**, 243–245 (2004).
- C. Weidenmaier, J. F. Kokai-Kun, E. Kulauzovic, T. Kohler, G. Thumm, H. Stoll, F. Götz, A. Peschel, Differential roles of sortase-anchored surface proteins and wall teichoic acid in *Staphylococcus aureus* nasal colonization. *Int. J. Med. Microbiol.* **298**, 505–513 (2008).
- S. Baur, M. Rautenberg, M. Faulstich, M. Faulstich, T. Grau, Y. Severin, C. Unger, W. H. Hoffmann, T. Rudel, I. B. Autenrieth, C. Weidenmaier, A nasal epithelial receptor for *Staphylococcus aureus* WTA governs adhesion to epithelial cells and modulates nasal colonization. *PLOS Pathog.* **10**, e1004089 (2014).
- V. Winstel, C. Liang, P. Sanchez-Carballo, M. Steglich, M. Munar, B. M. Bröker, J. R. Penadés, U. Nübel, O. Holst, T. Dandekar, A. Peschel, G. Xia, Wall teichoic acid structure governs horizontal gene transfer between major bacterial pathogens. *Nat. Commun.* **4**, 2345 (2013).
- X. Du, J. Larsen, M. Li, A. Walter, C. Slavetinsky, A. Both, P. M. Sanchez Carballo, M. Stegger, E. Lehmann, Y. Liu, J. Liu, J. Slavetinsky, K. A. Duda, B. Krämer, S. Heilbronner, C. Weidenmaier, C. Mayer, H. Rohde, V. Winstel, A. Peschel, *Staphylococcus epidermidis* clones express *Staphylococcus aureus*-type wall teichoic acid to shift from a commensal to pathogen lifestyle. *Nat. Microbiol.* **6**, 757–768 (2021).
- M. Schlag, R. Biswas, B. Krämer, T. Kohler, S. Zoll, W. Yu, H. Schwarz, A. Peschel, F. Götz, Role of staphylococcal wall teichoic acid in targeting the major autolysin Atl. *Mol. Microbiol.* **75**, 864–873 (2010).
- S. Brown, G. Xia, L. G. Luhachack, J. Campbell, T. C. Meredith, C. Chen, V. Winstel, C. Gekeler, J. E. Irazoqui, A. Peschel, S. Walker, Methicillin resistance in *Staphylococcus aureus* requires glycosylated wall teichoic acids. *Proc. Natl. Acad. Sci. U.S.A.* **109**, 18909–18914 (2012).
- M. L. Atilano, P. M. Pereira, J. Yates, P. Reed, H. Veiga, M. G. Pinho, S. R. Filipe, Teichoic acids are temporal and spatial regulators of peptidoglycan cross-linking in *Staphylococcus aureus*. *Proc. Natl. Acad. Sci. U.S.A.* **107**, 18991–18996 (2010).
- N. A. Caveney, F. K. Li, N. C. Strynadka, Enzyme structures of the bacterial peptidoglycan and wall teichoic acid biogenesis pathways. *Curr. Opin. Struct. Biol.* **53**, 45–58 (2018).
- B. Soldo, V. Lazarevic, D. Karamata, tagO is involved in the synthesis of all anionic cell-wall polymers in *Bacillus subtilis* 168. *Microbiology* **148**, 2079–2087 (2002).
- M. A. D'Elia, J. A. Henderson, T. J. Beveridge, D. E. Heinrichs, E. D. Brown, The N-acetylmannosamine transferase catalyzes the first committed step of teichoic acid assembly in *Bacillus subtilis* and *Staphylococcus aureus*. *J. Bacteriol.* **191**, 4030–4034 (2009).
- N. Ishimoto, J. L. Strominger, Polyribitol phosphate synthetase of *Staphylococcus aureus*. *J. Biol. Chem.* **241**, 639–650 (1966).
- S. Brown, Y. H. Zhang, S. Walker, A revised pathway proposed for *Staphylococcus aureus* wall teichoic acid biosynthesis based on *in vitro* reconstitution of the intracellular steps. *Chem. Biol.* **15**, 12–21 (2008).
- G. Xia, L. Maier, P. Sanchez-Carballo, M. Li, M. Otto, O. Holst, A. Peschel, Glycosylation of wall teichoic acid in *Staphylococcus aureus* by TarM. *J. Biol. Chem.* **285**, 13405–13415 (2010).
- D. Gerlach, Y. Guo, C. De Castro, S.-H. Kim, K. Schlatterer, F.-F. Xu, C. Pereira, P. H. Seeger, S. Ali, J. Codée, W. Sirisarn, B. Schulte, C. Wolz, J. Larsen, A. Molinaro, B. L. Lee, G. Xia, T. Stehle, A. Peschel, Methicillin-resistant *Staphylococcus aureus* alters cell wall glycosylation to evade immunity. *Nature* **563**, 705–709 (2018).
- V. Lazarevic, D. Karamata, The tagGH operon of *Bacillus subtilis* 168 encodes a two-component ABC transporter involved in the metabolism of two wall teichoic acids. *Mol. Microbiol.* **16**, 345–355 (1995).
- J. G. Swoboda, J. Campbell, T. C. Meredith, S. Walker, Wall teichoic acid function, biosynthesis, and inhibition. *Chembiochem* **11**, 35–45 (2010).
- Y. Kawai, J. Marles-Wright, R. M. Cleverley, R. Emmins, S. Ishikawa, M. Kuwano, N. Heinze, N. K. Bui, C. N. Hoyland, N. Ogasawara, R. J. Lewis, W. Vollmer, R. A. Daniel, J. Errington, A widespread family of bacterial cell wall assembly proteins. *EMBO J.* **30**, 4931–4941 (2011).
- F. K. K. Li, F. I. Rosell, R. T. Gale, J.-P. P. Simorre, E. D. Brown, N. C. J. Strynadka, Crystallographic analysis of *Staphylococcus aureus* LcpA, the primary wall teichoic acid ligase. *J. Biol. Chem.* **295**, 2629–2639 (2020).
- M. A. D'Elia, K. E. Millar, A. P. Bhavsar, A. M. Tomljenovic, B. Hutter, C. Schaab, G. Moreno-Hagelsieb, E. D. Brown, Probing teichoic acid genetics with bioactive molecules reveals new interactions among diverse processes in bacterial cell wall biogenesis. *Chem. Biol.* **16**, 548–556 (2009).

27. M. A. D'Elia, M. P. Pereira, Y. S. Chung, W. Zhao, A. Chau, T. J. Kenney, M. C. Sulavik, T. A. Black, E. D. Brown, Lesions in teichoic acid biosynthesis in *Staphylococcus aureus* lead to a lethal gain of function in the otherwise dispensable pathway. *J. Bacteriol.* **188**, 4183–4189 (2006).
28. M. Ramirez, A. Tomasz, Molecular characterization of the complete 23F capsular polysaccharide locus of *Streptococcus pneumoniae*. *J. Bacteriol.* **180**, 5273–5278 (1998).
29. A. L. Lovering, L. Y. C. Y.-C. Lin, E. W. Sewell, T. Spreter, E. D. Brown, N. C. J. J. Strynadka, Structure of the bacterial teichoic acid polymerase TagF provides insights into membrane association and catalysis. *Nat. Struct. Mol. Biol.* **17**, 582–589 (2010).
30. C. Litschko, M. R. Romano, V. Pinto, H. Claus, U. Vogel, F. Berti, R. Gerardy-Schahn, T. Fiebig, The capsule polymerase CslB of *Neisseria meningitidis* serogroup L catalyzes the synthesis of a complex trimeric repeating unit comprising glycosidic and phosphodiester linkages. *J. Biol. Chem.* **290**, 24355–24366 (2015).
31. C. Litschko, D. Oldrini, I. Budde, M. Berger, J. Meens, R. Gerardy-Schahn, F. Berti, M. Schubert, T. Fiebig, A new family of capsule polymerases generates teichoic acid-like capsule polymers in gram-negative pathogens. *MBio* **9**, 1–22 (2018).
32. D. R. Shaw, D. Mirelman, A. N. Chatterjee, J. T. Park, Ribitol teichoic acid synthesis in bacteriophage-resistant mutants of *Staphylococcus aureus*. *H. J. Biol. Chem.* **245**, 5101–5106 (1970).
33. F. Fiedler, L. Glaser, The synthesis of polyribitol phosphate. I. Purification of polyribitol phosphate polymerase and lipoteichoic acid carrier. *J. Biol. Chem.* **249**, 2684–2689 (1974).
34. M. P. Pereira, M. A. D'Elia, J. Trocynska, E. D. Brown, Duplication of teichoic acid biosynthetic genes in *Staphylococcus aureus* leads to functionally redundant poly(ribitol phosphate) polymerases. *J. Bacteriol.* **190**, 5642–5649 (2008).
35. T. C. Meredith, J. G. Swoboda, S. Walker, Late-stage polyribitol phosphate wall teichoic acid biosynthesis in *Staphylococcus aureus*. *J. Bacteriol.* **190**, 3046–3056 (2008).
36. M. P. Pereira, J. W. Schertzer, M. A. D'Elia, K. P. Koteva, D. W. Hughes, G. D. Wright, E. D. Brown, The wall teichoic acid polymerase TagF efficiently synthesizes poly(glycerol phosphate) on the TagB product lipid III. *ChemBioChem* **9**, 1385–1390 (2008).
37. A. P. Bhavsar, M. A. D'Elia, T. D. Sahakian, E. D. Brown, The amino terminus of *Bacillus subtilis* TagB possesses separable localization and functional properties. *J. Bacteriol.* **189**, 6816–6823 (2007).
38. K. N. Allen, S. Entova, L. C. Ray, B. Imperiali, Monotopic membrane proteins join the fold. *Trends Biochem. Sci.* **44**, 7–20 (2019).
39. D. M. Halaby, A. Poupon, J. P. Mornon, The immunoglobulin fold family: Sequence analysis and 3D structure comparisons. *Protein Eng.* **12**, 563–571 (1999).
40. D. Albesa-Jové, D. Giganti, M. Jackson, P. M. Alzari, M. E. Guerin, Structure-function relationships of membrane-associated GT-B glycosyltransferases. *Glycobiology* **24**, 108–124 (2014).
41. Q. Waheed, H. M. Khan, T. He, M. Roberts, A. Gershenson, N. Reuter, Interfacial aromatics mediating cation-π interactions with choline-containing lipids can contribute as much to peripheral protein affinity for membranes as aromatics inserted below the phosphates. *J. Phys. Chem. Lett.* **10**, 3972–3977 (2019).
42. C. L. Myers, F. K. K. Li, B.-M. Koo, O. M. El-Halawany, S. French, C. A. Gross, N. C. J. Strynadka, E. D. Brown, Identification of two phosphate starvation-induced wall teichoic acid hydrolases provides first insights into the degradative pathway of a key bacterial cell wall component. *J. Biol. Chem.* **291**, 26066–26082 (2016).
43. K. Schaefer, T. W. Owens, D. Kahne, S. Walker, Substrate preferences establish the order of cell wall assembly in *Staphylococcus aureus*. *J. Am. Chem. Soc.* **140**, 2442–2445 (2018).
44. A. S. Ramírez, J. Boilevin, A. R. Mehdioupi, G. Hummer, T. Darbre, J. L. Raymond, K. P. Locher, Structural basis of the molecular ruler mechanism of a bacterial glycosyltransferase. *Nat. Commun.* **9**, 445 (2018).
45. H. Schmidt, G. Hansen, S. Singh, A. Hanuszkiewicz, B. Lindner, K. Fukase, R. W. Woodard, O. Holst, R. Hilgenfeld, U. Mamat, J. R. Mesters, Structural and mechanistic analysis of the membrane-embedded glycosyltransferase WaaU required for lipopolysaccharide synthesis. *Proc. Natl. Acad. Sci. U.S.A.* **109**, 6253–6258 (2012).
46. J. W. Schertzer, A. P. Bhavsar, E. D. Brown, Two conserved histidine residues are critical to the function of the TagF-like family of enzymes. *J. Biol. Chem.* **280**, 36683–36690 (2005).
47. D. Giganti, D. Albesa-Jové, S. Urresti, A. Rodrigo-Unzueta, M. A. Martínez, N. Comino, N. Barilone, M. Bellinzoni, A. Chenal, M. E. Guerin, P. M. Alzari, Secondary structure reshuffling modulates glycosyltransferase function at the membrane. *Nat. Chem. Biol.* **11**, 16–18 (2015).
48. C. Martinez-Fleites, M. Proctor, S. Roberts, D. N. Bolam, H. J. Gilbert, G. J. Davies, Insights into the synthesis of lipopolysaccharide and antibiotics through the structures of two retaining glycosyltransferases from family GT4. *Chem. Biol.* **13**, 1143–1152 (2006).
49. J. K. Lassila, J. G. Zalatan, D. Herschlag, Biological phosphoryl-transfer reactions: Understanding mechanism and catalysis. *Annu. Rev. Biochem.* **80**, 669–702 (2011).
50. L. L. Lairson, B. Henrissat, G. J. Davies, S. G. Withers, Glycosyltransferases: Structures, functions, and mechanisms. *Annu. Rev. Biochem.* **77**, 521–555 (2008).
51. J. W. Schertzer, E. D. Brown, Use of CDP-glycerol as an alternate acceptor for the teichoic acid polymerase reveals that membrane association regulates polymer length. *J. Bacteriol.* **190**, 6940–6947 (2008).
52. J. W. Schertzer, E. D. Brown, Purified, recombinant TagF protein from *Bacillus subtilis* 168 catalyzes the polymerization of glycerol phosphate onto a membrane acceptor in vitro. *J. Biol. Chem.* **278**, 18002–18007 (2003).
53. S. Sobhanifar, L. J. Worrall, D. T. King, G. A. Wasney, L. Baumann, R. T. Gale, M. Nosella, E. D. Brown, S. G. Withers, N. C. J. Strynadka, Structure and mechanism of *Staphylococcus aureus* TarS, the wall teichoic acid β-glycosyltransferase involved in methicillin resistance. *PLOS Pathog.* **12**, e1006067 (2016).
54. L. Holm, P. Rosénström, Dali server: Conservation mapping in 3D. *Nucleic Acids Res.* **38**, W545–W549 (2010).
55. M. Zolli, D. J. Kobic, E. D. Brown, Reduction precedes cytidyl transfer without substrate channeling in distinct active sites of the bifunctional CDP-ribitol synthase from *Haemophilus influenzae*. *Biochemistry* **40**, 5041–5048 (2001).
56. S. Lyskov, F. C. Chou, S. Ó. Conchúir, B. S. Der, K. Drew, D. Kuroda, J. Xu, B. D. Weitzner, P. D. Renfrew, P. Sripathadevong, B. Borgo, J. J. Havranek, B. Kuhlman, T. Kortemme, R. Bonneau, J. J. Gray, R. Das, Serverification of molecular modeling applications: The rosetta online server that includes everyone (ROSIE). *PLOS ONE* **8**, 5–7 (2013).
57. E. F. Pettersen, T. D. Goddard, C. C. Huang, G. S. Couch, D. M. Greenblatt, E. C. Meng, T. E. Ferrin, UCSF Chimera—A visualization system for exploratory research and analysis. *J. Comput. Chem.* **25**, 1605–1612 (2004).
58. P. D. Adams, P. V. Afonine, G. Bunkóczki, V. B. Chen, I. W. Davis, N. Echols, J. J. Headd, L. W. Hung, G. J. Kapral, R. W. Grosse-Kunstleve, A. J. McCoy, N. W. Moriarty, R. Oeffner, R. J. Read, D. C. Richardson, J. S. Richardson, T. C. Terwilliger, P. H. Zwart, PHENIX: A comprehensive Python-based system for macromolecular structure solution. *Acta Crystallogr. D Biol. Crystallogr.* **66**, 213–221 (2010).
59. P. Emsley, B. Lohkamp, W. G. Scott, K. Cowtan, Features and development of Coot. *Acta Crystallogr. D Biol. Crystallogr.* **66**, 486–501 (2010).
60. W. Kabsch, XDS. *Acta Crystallogr. D Biol. Crystallogr.* **66**, 125–132 (2010).
61. P. Grochulski, M. N. Fodje, J. Gorin, S. L. Labiuk, R. Berg, Beamline 08ID-1, the prime beamline of the Canadian macromolecular crystallography facility. *J. Synchrotron Radiat.* **18**, 681–684 (2011).
62. A. J. McCoy, R. W. Grosse-Kunstleve, P. D. Adams, M. D. Winn, L. C. Storoni, R. J. Read, Phaser crystallographic software. *J. Appl. Cryst.* **40**, 658–674 (2007).
63. P. V. Afonine, R. W. Grosse-Kunstleve, N. Echols, J. J. Headd, N. W. Moriarty, M. Mustyakimov, T. C. Terwilliger, A. Urzhumtsev, P. H. Zwart, P. D. Adams, Towards automated crystallographic structure refinement with phenix.refine. *Acta Crystallogr. D Biol. Crystallogr.* **68**, 352–367 (2012).
64. E. F. Pettersen, T. D. Goddard, C. C. Huang, E. C. Meng, G. S. Couch, T. I. Croll, J. H. Morris, T. E. Ferrin, UCSF ChimeraX: Structure visualization for researchers, educators, and developers. *Protein Sci.* **30**, 70–82 (2021).
65. R. A. Laskowski, M. B. Swindells, LigPlot+: Multiple ligand-protein interaction diagrams for drug discovery. *J. Chem. Inf. Model.* **51**, 2778–2786 (2011).
66. X. Robert, P. Gouet, Deciphering key features in protein structures with the new ENDscript server. *Nucleic Acids Res.* **42**, W320–W324 (2014).
67. A. R. Möl, M. S. Castro, W. Fontes, NetWheels: A web application to create high quality peptide helical wheel and net projections. 1–7 (2018).
68. M. A. Lomize, I. D. Pogozheva, H. Joo, H. I. Mosberg, A. L. Lomize, OPM database and PPM web server: Resources for positioning of proteins in membranes. *Nucleic Acids Res.* **40**, 370–376 (2012).

Acknowledgments: We thank beamline staff for assistance with x-ray data collection at the CLS, APS, and ALS synchrotron facilities. CLS, a national research facility of the University of Saskatchewan, is supported by the Canada Foundation for Innovation, the Natural Sciences and Engineering Research Council, the National Research Council, the Canadian Institutes of Health Research, the Government of Saskatchewan, and the University of Saskatchewan. The content is solely the responsibility of the authors and does not necessarily represent the official views of the National Institutes of Health. This research used resources of the APS, a U.S. Department of Energy (DOE) Office of Science User Facility operated for the DOE Office of Science by Argonne National Laboratory under contract no. DE-AC02-06CH11357. ALS, a U.S. DOE Office of Science User Facility under contract no. DE-AC02-05CH11231, is supported in part by the ALS-ENABLE program funded by the National Institutes of Health, National Institute of General Medical Sciences, grant P30 GM124169-01. We thank C. Atkinson, F. Rossmann, and J. Felt for cryo-EM grid screening at HRTEM. HRTEM is funded by the Canadian Foundation of Innovation, BC Knowledge Development Fund, and UBC. A portion of this research was supported by NIH grant U24GM129547, performed at the PNCC at OHSU, and accessed through EMSL (grid.436923.9), a DOE Office of Science User Facility sponsored by the Office of Biological and Environmental Research. We thank T. Humphreys and H. Scott for cryo-EM data collection at PNCC. **Funding:** This work was supported by the Natural Sciences and Engineering Research Council (to F.K.K.L.), the Mitacs Accelerate Fellowship (to F.K.K.L.), the Canadian Institutes of Health Research (to N.C.J.S., R.T.G., and E.D.B.), the Howard Hughes Medical Institute International Senior Scholar program (to N.C.J.S.), the Canadian Foundation

of Innovation (to N.C.J.S. and E.D.B.), the Canada Research Chairs program (to N.C.J.S. and E.D.B.), and the British Columbia Knowledge Development Fund (to N.C.J.S.). **Author contributions:** Conceptualization: F.K.K.L. and N.C.J.S. Methodology: F.K.K.L. Validation: F.K.K.L. Formal analysis: F.K.K.L. and L.J.W. Investigation: F.K.K.L., L.J.W., and R.T.G. Resources: R.T.G., E.D.B., and N.C.J.S. Writing—original draft: F.K.K.L. Writing—review and editing: F.K.K.L., L.J.W., R.T.G., E.D.B., and N.C.J.S. Visualization: F.K.K.L. Supervision: E.D.B. and N.C.J.S. Project administration: N.C.J.S. Funding acquisition: E.D.B. and N.C.J.S. **Competing interests:** The authors declare that they have no competing interests. **Data and materials availability:** All data needed to evaluate the conclusions in the paper are present in the paper and/or the Supplementary Materials. The cryo-EM maps and model of TarL H300N have been deposited in

the EMDB and PDB under accession codes EMD-43084 (two tetramers with CHAPS micelle), EMD-43083 (single tetramer), and PDB 8VA1 (single tetramer). The coordinates and structure factors of crystallographic data have been deposited in the PDB with accession codes 8V33 (TarL NTD) and 8V34 (TarK NTD).

Submitted 28 June 2023

Accepted 23 January 2024

Published 28 February 2024

10.1126/sciadv.adj3864